Mathematical Biosciences and Engineering

http://www.aimspress.com/journal/mbe

MBE, 20(2): 2408–2438.
DOI: 10.3934/mbe.2023113
Received: 06 August 2022
Revised: 27 October 2022
Accepted: 30 October 2022
Published: 21 November 2022

Research article

On the significance of membrane unfolding in mechanosensitive cell spreading: Its individual and synergistic effects

Magdalena A. Stolarska[1,*] **and Aravind R. Rammohan**[2]

[1] Department of Mathematics, 2115 Summit Ave., University of St. Thomas, St. Paul, MN 55105, USA

[2] Corning Life Sciences, Corning Inc., 836 North St, Tewksbury, MA 01876, USA

* **Correspondence:** Email: mastolarska@stthomas.edu.

Abstract: Mechanosensitivity of cell spread area to substrate stiffness has been established both through experiments and different types of mathematical models of varying complexity including both the mechanics and biochemical reactions in the cell. What has not been addressed in previous mathematical models is the role of cell membrane dynamics on cell spreading, and an investigation of this issue is the goal of this work. We start with a simple mechanical model of cell spreading on a deformable substrate and progressively layer mechanisms to account for the traction dependent growth of focal adhesions, focal adhesion induced actin polymerization, membrane unfolding/exocytosis and contractility. This layering approach is intended to progressively help in understanding the role each mechanism plays in reproducing experimentally observed cell spread areas. To model membrane unfolding we introduce a novel approach based on defining an active rate of membrane deformation that is dependent on membrane tension. Our modeling approach allows us to show that tension-dependent membrane unfolding plays a critical role in achieving the large cell spread areas experimentally observed on stiff substrates. We also demonstrate that coupling between membrane unfolding and focal adhesion induced polymerization works synergistically to further enhance cell spread area sensitivity to substrate stiffness. This enhancement has to do with the fact that the peripheral velocity of spreading cells is associated with contributions from the different mechanisms by either enhancing the polymerization velocity at the leading edge or slowing down of the retrograde flow of actin within the cell. The temporal evolution of this balance in the model corresponds to the three-phase behavior observed experimentally during spreading. In the initial phase membrane unfolding is found to be particularly important.

Keywords: cell spreading; cell-substrate interaction; membrane unfolding; biomechanics; mechanosensitivity

1. Introduction

The ability for cells to sense and respond to the mechanical properties of their environment plays a critical role in processes such as the differentiation of stem cells, cell motility and the development of cancer [1–3]. This process, termed mechanosensing, allows cells to adapt to changes in conditions of their environment. One important example of mechanosensing is cell spreading when cells with an initially round morphology flatten and extend on a substrate. Experiments of cell types such as fibroblasts [4,5], hMSCs [6,7], endothelial cells [8] and osteoblastic cells [9] all show that cells obtain larger spread areas on stiffer substrates. As Figure 1 illustrates, spread areas increase significantly on stiffer substrates and the amount of increase depends on cell type. The cell spread area for hMSCs increases approximately 300% as the gel stiffness increases from 1 kPa to 70 GPa [6]. Similarly, for NIH-3T3 fibroblasts the cell spread area increases approximately 200% as the substrate stiffness increases from 1 kPa to that of glass (approximately 50 GPa) [5]. By starting with a mechanistic model of cell-substrate interaction during spreading and successively adding various other model components, in this work, we aim to unravel which biomechanical mechanisms are required for cells to obtain these large differences in cell spread area as they sense the mechanical properties of the substrate. We demonstrate that the unfolding of membrane reserves is required for cells to achieve a 200–300% increase in cell spread area on stiff substrates. To accommondate such a large increase in cell spread area large membrane deformations are required. With the membrane properties reported in the literature, the absence of membrane unfolding would lead to significant membrane tension early in the spreading process, which would in turn inhibit further spreading.

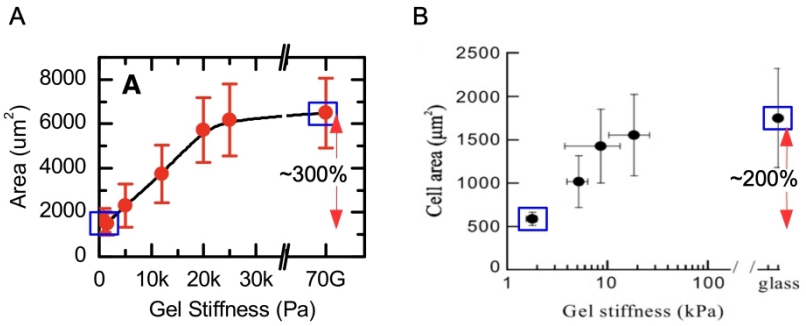

Figure 1. Cell spread area dependence on substrate Young's modulus determined experimentally. (A) Cell areas for hMSCs [6] (reproduced with permission). (B) Cell areas for NIH-3T3 fibroblasts [5] (reproduced with permission). In both cases, the noted percent increase is calculated by taking the difference in the spread areas in blue boxes and dividing by the smallest spread area.

Mechanosensing is initiated at integrin-based cell-substrate attachments. Via mediation by a variety of accessory proteins such as talin, vinculin, Src and focal adhesion (FA) kinase, integrins transmit force to the cytoskeleton and initiate various signaling cascades [10, 11]. Integrins form catch bonds with fibronectin [12, 13], an extracellular matrix protein, and the strengthening of nascent adhesions into mature FAs is modulated by applied forces arising from integrin-fibronectin bonds and intrcellular tension from actomyosin contractions [11]. Individual FA size and the total amounts of activated

integrins in a spreading cell also depends on substrate stiffness [4, 14]. By regulating the size, strength, engagement and disengagement of cell-substrate attachments, i.e., by activating the "actin clutch", a cell can locally regulate movement and force generation in response to mechanical cues from its environment [15]. This actin clutch mechanism also plays a role in the sensitivity of cell spread areas to substrate stiffness [16, 17].

During spreading, the cell area increases rapidly at first (Phase P1), then the rate of increase slows down (Phase P2), then finally plateaus [18,19]. The lipid bilayer of the cell membrane is extremely stiff and can rupture when its stretch reaches a threshold of 2–4% [20, 21]. However, it has been observed that spreading requires that the membrane area increases by at least 20–30% [22], which is far above this threshold. To allow for the large membrane deformations required for motility, spreading and mitosis, this complex cellular structure consisting of folds, such as caveolae, filopodia and invaginations, unfolds to allow for cellular expansion. The cell also contains tension-controlled membrane reservoirs that can be trafficked from the cell interior to the membrane via exocytosis [22–25]. Unfolding occurs during the rapid spreading Phase P1, while membrane tension that builds up in the initial phase of cell spreading results in exocytosis of membrane reservoirs in Phase P2, initiates myosin contractility and initiates the formation of new nascent adhesions [26, 27]. Experimental results point to the complexity of cell spreading and to the coupling of a variety of biochemical and biomechanical processes that must exist in order for mechanosensitivity during spreading to occur. Notably, one such process is membrane unfolding and exocytosis. While to date there is no experimental work that considers how the inhibition of membrane unfolding affects mechanosensitivity, it has been shown that membrane unfolding is critical for bleb formation and inhibiting the release of membrane invaginations reduces the ability of cells to form blebs and translocate [25].

There are several mathematical models of cell spreading on 2D substrates, some of which focus on mechanosensing of substrate material properties. Several of these models do not include the cell membrane, and no models to date account for the role of active membrane deformations, such as unfolding, in mechanosensitivity. Using a simple, one-dimensional model [28] shows that the balance between the polymerization rate and the retrograde flow is modified with substrate stiffness. A similar one-dimensional model [29] shows that substrate viscosity works to stiffen softer substrates and maximize cell spread areas. Further, a more detailed two dimensional model [30] recapitulates the experimentally observed cell spread area sensitivity to substrate stiffness by speculating that mechanosensing is modulated by the balance of a pushing force arising from membrane deformation and a pulling force driven by cell-substrate adhesion. Using a variety of approaches, such as a Cellular Potts Model [31], energy balance principles [32], discrete structure interaction [33] and continuum modeling [34], other two-dimensional models show that the coupling between FA strengthening and polarization of stress fibers leads to increased spread area and increased anisotropy on stiffer substrates. Other models include simulations of three-dimensional spreading cells and investigate the dynamics of cell spreading and the relocation of membrane-bound proteins during spreading [35–37]. A benefit of modeling in three dimensions is that one can include more details on the spatial localization of subcellular components during spreading [38]. Of this theoretical work, the models in [30, 33] account for membrane deformation during spreading. Effects of membrane softening are accounted for in [39], where it is shown that that the cell spread area increases when membrane stiffness decreases. Using an energy minimization approach, the authors of [40] model the effects of membrane folds in bleb formation by formulating an expression for membrane tension that is dependent on the membrane area fraction held

in folds.

Our work adds to the body of research on mechanosensing during cell spreading by incorporating a model of membrane unfolding / exocytosis that is dependent on membrane tension and FA activity. Moreover, our approach of layering model components provides insight into which biophysical mechanisms contribute most to mechanosensitivity during spreading and how the coupling between mechanisms affects mechanosensitivity. This approach is to start with a mechanistic model of cell substrate interaction and sequentially layer model components that incorporate stress-dependent FA evolution, FA-dependent actin polymerization, membrane unfolding/exocytosis and contractility. We run simulations as each layer is added to understand how each modeling component contributes to the amplification of the cell spread area in mechanosensing of substrate stiffness, and, as we add modeling components, we verify that the addition of each layer is consistent with biological reality by comparing biophysical aspects of a spreading cell to experimental results. Our modeling approach shows that tension-dependent membrane unfolding plays the most significant role in mechanosensitive cell spreading, shows that the coupling between mechanisms is required to obtain large differences in cell spread areas on soft and stiff substrates and illustrates how protrusive and retractive activity at the cell edge changes with each mechanism to result in the experimentally observed temporal dynamics of spreading.

2. Methods

2.1. Overview of modeling approach

To investigate the role of various biophysical mechanisms on a cell's sensitivity to substrate stiffness during spreading we model the cell as a two-dimensional axisymmetric body and start with a model that accounts only for mechanical interactions between a spreading cell and a linearly elastic substrate, whose stiffness is specified by its Young's modulus*. We then successively layer additional mechanisms that are known to affect mechanosensing during cell spreading. We call the starting model that accounts for only mechanical interactions the minimalistic mechanical model (MM model). In the MM model (and all subsequent additions to it), we do not separately model various actin components, such as the cortex, lamellum, lamellipodium and stress fibers. Rather, we have a unified representation of the cell and treat the cell interior as a viscous fluid that is surrounded by a viscoelastic membrane. Such a homogenization of intracellular components has been regularly used when modeling whole-cell movement (see, for example, [30,41]). In addition, experimentally measured material properties of the cell also assume that the cell behaves as a homogeneous continuum [42]. We account for the various actin regions by specifying a polymerization velocity and, in the Contract model (described later), a local active contraction. The interaction between the cell and substrate is modeled as a viscous drag. In the MM model, the drag coefficient between the two entities is held constant. An overview of the MM model and all other components that we layer is described in Figure 2A. In Figure 2A we also indicate how the models are layered via solid black arrows.

*Experimental literature often refers to the Young's modulus as either stiffness or rigidity. In this work we use the term stiffness or Young's modulus.

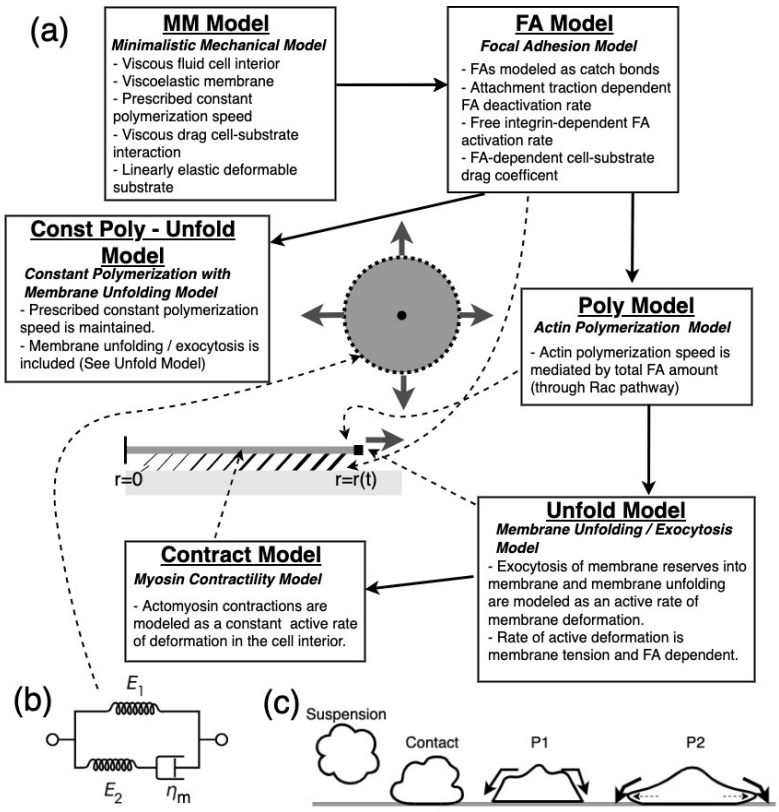

Figure 2. Overview of modeling approach. (A) A description of each model component used. Solid straight black arrows indicate flow of model component layering. Starting with the MM model, additional components are successively added. Thin dashed arrows indicate which cellular region a model component affects. (B) Spring-dashpot system for standard solid model, which is used to model the material response of the cell membrane. (C) Phases of cell spreading as viewed from the side. Upon contact with a ligand-coated surface from suspension, a cell flattens and forms nascent adhesions. To allow for more membrane expansion, as membrane tension increases, the membrane unfolds (Phase P1) and then releases membrane reserves via exocytosis (Phase P2) [24]. Black solid arrows point to location of membrane tension development as assumed by our model. Dashed arrows represent exocytosis of membrane reserves.

Because of the critical role of cell-substrate adhesions in mechanosensing, the first model added to the MM model is a model of FA evolution (FA model). In the FA model we add attachment-traction-dependent FA evolution and an FA-dependent cell-substrate drag coefficient. On top of this we layer an attachment-dependent actin polymerization model (Poly model). To this, we add our model of membrane unfolding / exocytosis (Unfold model). Lastly, we account for the affects of myosin-induced contraction in the Contract model. To determine the individual effects of membrane unfolding and attachment-dependent actin polymerization on cell spread areas, to the FA model we separately add a model of membrane exocytosis / unfolding (resulting in the Const Poly - Unfold model). In the sections below, we describe the assumptions and governing equations of each model component.

2.2. MM model for the cell and model of substrate deformation

The MM model accounts for only mechanical interactions between a spreading cell and the underlying substrate. In the MM model, the cell interior, which we assume consists mainly of actin in various states, is treated as a viscous fluid that is surrounded by a viscoelastic membrane. We assume an axisymmetric quasi-steady state for the cell, which results in the following equilibrium equation for the cell interior with the cell-substrate attachment force $\mathbf{f}_{\text{attach}}$:

$$\nabla \cdot \boldsymbol{\sigma}_c = -\mathbf{f}_{\text{attach}} \tag{2.1}$$

The Cauchy stress in the actin network is represented by $\boldsymbol{\sigma}_c$ and given by

$$\boldsymbol{\sigma}_c = 2\mu \mathbf{D}_c + \lambda \text{Tr}(\mathbf{D}_c)\mathbf{I} \tag{2.2}$$

where $\mathbf{D}_c = \frac{1}{2}(\nabla \mathbf{v}_c + \nabla^T \mathbf{v}_c)$ is the rate of deformation tensor and $\text{Tr}(\mathbf{D}_c)$ is the trace of this tensor. The parameter μ is the shear viscosity and λ represents additional contributions to bulk viscosity equaling $\mu + \lambda$ in two-dimensional analysis. Because the entire actin network is represented by this viscous fluid model and this network can locally vary in density due to variation in accessory proteins and composition [43–45], we do not assume that the fluid is incompressible and therefore do not include a pressure term in (2.2). Given our assumption that the spreading cell is axisymmetric, we formulate the equations above in polar coordinates and neglect any variations in the angular direction. This allows us to rewrite (2.1) and (2.2) as the following system of equations for the radial velocity of intracellular actin $v_c(r,t)$, radial component of the intracellular Cauchy stress $\sigma_r(r,t)$ and angular component of this stress $\sigma_\theta(r,t)$

$$\frac{\partial \sigma_r}{\partial r} + \frac{1}{r}\Big(\sigma_r - \sigma_\theta\Big) + f_{\text{attach}} = 0 \tag{2.3}$$

$$\sigma_r - K\Big(\frac{\partial v_c}{\partial r}\Big) - \lambda\Big(\frac{v_c}{r}\Big) = 0 \tag{2.4}$$

$$\sigma_\theta - K\Big(\frac{v_c}{r}\Big) - \lambda\Big(\frac{\partial v_c}{\partial r}\Big) = 0 \tag{2.5}$$

where $K = 2\mu + \lambda$. By setting $\lambda = 0$, from this point forward we assume that the radial stress depends only on radial strain and angular stress on angular strain. Further justification of setting this parameter to zero is based on a lack of experimental evidence for its value and, as shown in Figure S2 and its caption, our numerical simulations indicate that setting it to a nonzero values does not significantly affect the numerical results or our essential conclusions.

As has been done by several others [41, 46, 47], we assume a viscous drag for cell-substrate interaction. The physical interactions between a motile cell and a two-dimensional substrate are complex, but a viscous drag approach is a valid approach for capturing the binding and unbinding for activated integrins with substrate ligands that occurs during motility [48, 49]. In our model, we assume that the cell-substrate attachment force has the form

$$f_{\text{attach}} = -\eta_{\text{att}}(v_c - v_s). \tag{2.6}$$

In (2.6), η_{att} is the viscous drag coefficient and v_s is a substrate velocity.

The force f_{attach} is acting on both the cell and the substrate in opposite directions. It is proportional to v_c and to v_s, and it is time-dependent. While v_c is directly involved in the model of the cell and is evaluated in the solution process, v_s is not. The absence of v_s in the solution process is related to the quasi-static, linearly elastic model of the substrate. In this model, f_{attach} produces instantaneous displacements that are proportional to f_{attach}, rather than velocities. So, on the one hand the viscous cell-substrate interaction model specified in (2.6) defines f_{attach} to be proportional to v_s, but on the other hand our linear-elastic model of the substrate makes it proportional to u_s. Thus in (2.6) we use a "surrogate" substrate velocity defined as

$$v_s \;=\; \frac{\alpha_a}{\Delta t} u_s \tag{2.7}$$

where Δt is a time step introduced for dimensional consistency and α_a is a proportionality parameter ensuring that $(v_c - v_s) > 0$. This inequality must be satisfied for the substrate to provide a drag for the spreading cell. In our calculations, we set Δt to the time step of our simulation. However, any reference time can be used for this parameter with an appropriate adjustment of α_a. We see this as an original way of handling a viscous drag interaction between an elastic solid and a viscous material.

We recognize that this approach makes v_s dependent on the modeling assumptions. However, we keep Δt and α_a fixed throughout all of our numerical simulations, while u_s changes with the variation of other parameters of the model, allowing v_s to serve as measure of the substrate velocity.

We fix the cell at $r = 0$ (see Figure 2). At the moving boundary of the cell at $r = r(t)$ we assume that actin polymerizes at a radial velocity v_{poly} and the polymerization of actin stretches the cell membrane. The resulting force applied to the actin network is oriented toward the cell interior and leads to retrograde flow of the actin network at a velocity v_c. Therefore, the velocity of the periphery of the spreading cell is given by $v_{periph} = v_{poly} + v_c$. Note that v_{poly} is always positive and, due to the orientation of the membrane force, v_c is always negative. However, when we refer to the actin retrograde flow *speed*, we assume that this is a positive quantity.

We model the membrane as a standard viscoelastic solid, as illustrated in Figure 2B. We set the material properties of the cell membrane to be those of the lipid bilayer. The lipid bilayer is very stiff with a small viscosity [50], and the material response can be adequately modeled as purely elastic. However, there are experimental results [51], as well as mathematical models [52], that treat the membrane as viscoelastic. The additional benefit of modeling the membrane as a viscoelastic material is that including the viscosity term in our model stabilizes abrupt jumps in membrane tension that would otherwise occur during numerical simulations.

Cell spreading can lead to large membrane deformations and, in the analysis, we assume an Almansi-Hamel finite strain measure, ε_{mem}:

$$\varepsilon_{mem} \;=\; \frac{1}{2}\Big(1 - \Big(\frac{R_0}{r}\Big)^2\Big), \tag{2.8}$$

where R_0 is the initial cell radius at $t = 0$ and $r = r(t)$ is the cell radius at time t. The membrane strain rate that follows is

$$\dot{\varepsilon}_{mem} \;=\; \frac{R_0^2}{r^3} v_{periph} \;=\; \frac{R_0^2}{r^3}(v_{poly} + v_c). \tag{2.9}$$

In terms of the strain and strain rate, the standard viscoelastic solid constitutive equation for the

membrane force, σ_{mem}, is given by

$$\dot{\sigma}_{mem} = (E_1 + E_2)\dot{\varepsilon}_{mem} + \frac{E_1 E_2}{\eta_m}\varepsilon_{mem} - \frac{E_2}{\eta_m}\sigma_{mem}. \tag{2.10}$$

Here, E_1 and E_2 are the two spring constants describing the elastic properties of the membrane, and η_m is the membrane viscosity. The force σ_{mem} effectively serves as a boundary condition on the free boundary of the actin network.

The substrate is coupled to the cell via the cell-substrate attachment force. As we do for the cell, we assume that the substrate is axisymmetric, and the equilibrium equation for its radial displacement $u_s(r,t)$ is given by

$$C_s\frac{\partial}{\partial r}\Big(\frac{\partial u_s}{\partial r} + \nu_p\frac{u_s}{r}\Big) + \frac{C_s(1-\nu_p)}{r}\Big(\frac{\partial u_s}{\partial r} - \frac{u_s}{r}\Big) - f_{\text{attach}} = 0. \tag{2.11}$$

Here, $C_s = \frac{E_s}{1-\nu_p^2}$, where E_s is the Young's modulus of the substrate and ν_p is its Poisson ratio. Both endpoints of the substrate computational domain are fixed. Throughout the simulations, the radius of the substrate remains significantly larger than that of the spreading cell to minimize the effects of the substrate boundary on the mechanics of cell spreading.

All parameter values used in the MM model are listed in Table S1 of the supplementary material.

2.3. FA model

The interface between the cell and substrate is where the mechanical properties of the substrate are translated into a complex system of biochemical responses that modulate many aspects of cell motility. The FA model aims to encapsulate the details of this complex mechano-chemical interaction into a higher level model. Experimental results indicate that integrin-ligand interactions function as catch bonds, whose lifetimes increase with applied force [53]. We base the FA model on earlier experimental and modeling work and also assume that the integrin-ligand bond is a catch bond. In both [53] and [31], the integrin-ligand bond is modeled using a double exponential term that captures a decrease in the FA degradation as force on the bond increases as well as an increase in FA degradation at sufficiently high forces. For tractability of the whole cell-substrate model we are considering here, we use the approach of [54] and model the catch bond with a single exponential. In addition, we make the following two assumptions that have also been made in earlier work [31,54]: 1) there is a finite pool of available free integrins that are able to bond with substrate ligands, and 2) that integrin clusters are able to contain a finite number of integrin molecules. In our model, the variable $\phi(r,t)$ accounts for the cell-substrate adhesion complex consisting of integrins and other accessory proteins, which, from here forward, we refer to as the FA complex. The evolution equation for ϕ is given by

$$\frac{d\phi}{dt} = D\nabla^2\phi + k_{on}^0(N_{max} - \phi^{TOT})(\phi_{max} - \phi) - k_{off}^0 e^{-k_a|f_{attach}|}\phi. \tag{2.12}$$

In (2.12), the derivative on the left-hand side is a material derivative, and D is a diffusion coefficient whose numerical value is small, but it is retained here as it is known to enhance numerical stability. In the FA activation, the rate term k_{on}^0 is a base activation rate, N_{max} is a measure of the total number of free FA complex molecules present in the cell and ϕ_{max} is a measure of the maximum concentration of ϕ that is allowed at a specific point in the FA cluster. $\phi^{TOT}(t)$ is the total number of FA complex

molecules in the cell, and this quantity is calculated by integrating $\phi(r,t)$ over the current cell area. The base degradation rate is given by k_{off}^0. The exponential term represents a catch bond by lowering the degradation rate as the force in the FA-ligand attachment increases, and k_a is the feedback parameter from the attachment force to the degradation rate. When we add myosin-induced contractility to the model, we slightly modify (2.12) and also add an intracellular tension component to the FA complex degradation (see Section 2.6).

Local variations of the FA complex will result in spatial variation in the formation of cell-substrate attachments, and here we assume that the attachment strength increases with local FA complex amounts. We model this as a ϕ-dependent attachment drag coefficient given by the saturating function

$$\eta_{att}(\phi) \;=\; \eta_a^0 + \eta_{max}\frac{\left(\frac{\phi}{\phi_0}\right)^2}{1+\left(\frac{\phi}{\phi_0}\right)^2}. \tag{2.13}$$

The parameter η_a^0 is the baseline attachment strength and η_{max} is the maximum amount by which the baseline attachment strength can increase. ϕ_0 is a reference FA complex amount. A similar model for attachment strength dependence on FA complex density was used in [55].

All parameter values used in the FA model are in Table S2 of the supplementary material. We note that several of these parameters are defined here for the first time. In selecting those parameters, our goal is to show that the FA model compares qualitatively to experimental results. We realize that an alternate set of parameters might lead to a comparable set of qualitative results. This is explained further in 3.2 of Results.

2.4. Actin polymerization model

Cellular protrusion via actin polymerization has been shown to be mediated by integrin-ligand attachments [56,57]. Specifically, attachments at appropriate levels of ligand concentrations induce activation of Rac1, whose downstream affect is stable polymerization of actin at the membrane. In the Poly model, the FA complex serves as a proxy for Rac1, and we assume that the radial actin polymerization velocity, v_{poly} depends on the total amount of FA complex in the cell, $\phi^{TOT}(t)$, such that

$$v_{poly} \;=\; \frac{v_{poly}^0 + v_{poly}^{max}\alpha_v\phi^{TOT}}{1+\alpha_v\phi^{TOT}} \tag{2.14}$$

where v_{poly}^0 and v_{poly}^{max} is the minimum polymerization velocity and the maximum amount by which the polymerization velocity can increase, respectively. The tuning parameter α_v controls the sensitivity of v_{poly} to the FA complex. The form of (2.14) is based on the polymerization velocity function in [58].

We make the actin polymerization velocity depend on ϕ^{TOT} rather than the local value of ϕ at the cell periphery because activation of Rac1 occurs at FA sites, and this differs from the location of Rac1 action, which is at the cell periphery [59]. Therefore, the activation of stable actin protrusions via integrins is a nonlocal process with several intermediary effectors. To simplify these details in our system level model, we chose to represent this nonlocality by having v_{poly} depend on the total FA complex in the cell ϕ^{TOT}.

All parameter values used in the Poly model are in Table S3 of the supplementary material.

2.5. Membrane unfolding / exocytosis model

The membrane tension that builds up in the initial phases of cell spreading induces membrane unfolding and exocytosis (which, for simplicity, henceforth we will refer to collectively as 'unfolding'), and we aim to capture these two processes in the Unfold model by modeling them as an active rate of deformation of the cell membrane. In the approach described below, we define a novel algorithm for determining the active rate of membrane deformation.

In general, active deformations represent any local changes in shape that are driven by active intracellular processes, such as the polymerization of actin or actomyosin contractions. Passive deformations result from forces applied to the cell, including those from cell-substrate attachments, and from incompatibilities in local active deformations. A representation of active and passive deformations is illustrated in Figure S1A. In finite deformation processes taking place in the phenomena discussed here, a multiplicative decomposition of the deformation gradient is typically employed to define passive and active components of deformation [60]. However, when the passive deformation is small, an additive decomposition of the strain is appropriate even though the active deformation is still large [61]. Here, due to large membrane stiffness, the passive deformation of the membrane is small relative to the active deformation representing unfolding. Therefore, we additively decompose the strain in the cell membrane into a passive component, ε^p_{mem}, and an active component, ε^A_{mem}, such that

$$\varepsilon_{mem} \;=\; \varepsilon^p_{mem} + \varepsilon^A_{mem}. \tag{2.15}$$

A justification of the additive decomposition used here and an explanation of how ε^A_{mem} is defined are provided in Section 1 of the supplementary material. The rate of active deformation represents the rate of membrane unfolding and is denoted by D^A_{mem}. The total strain rate is therefore also decomposed additively into active and passive parts:

$$\dot{\varepsilon}_{mem} \;=\; \dot{\varepsilon}^p_{mem} + D^A_{mem}. \tag{2.16}$$

The local active deformation is always assumed to be stress-free. Any stresses in the membrane result from either applied forces or incompatible active deformations and are related to the passive component of the strain. This leads to the following form of the constitutive equation (2.10) for the membrane:

$$\dot{\sigma}_{mem} \;=\; (E_1 + E_2)(\dot{\varepsilon}_{mem} - D^A_{mem}) + \frac{E_1 E_2}{\eta_m}(\varepsilon_{mem} - \varepsilon^A_{mem}) - \frac{E_2}{\eta_m}\sigma_{mem} \tag{2.17}$$

There are various ways of using (2.17) in the solution process, depending on what information is given in the model. Each way recognizes the fact that, for ε_{mem}, ε^A_{mem} and σ_{mem} known at time t, this equation provides a relationship between the corresponding rates, $\dot{\varepsilon}_{mem}$, D^A_{mem} and $\dot{\sigma}_{mem}$.

We base our algorithm on experimental results that indicate that there is interaction between integrins and the membrane during cell spreading [62]. The detailed nature of this interaction is unknown. However, it is understood that membrane tension is related to adhesion formation and placement and that tension also activates membrane unfolding [27]. Therefore, we first specify $\dot{\varepsilon}_{mem}$ and $\dot{\sigma}_{mem}$ and compute D^A_{mem} using (2.17), thereby determining an active rate of membrane deformation that is dependent on the rate of change of membrane tension. This approach is meant to reflect the experimentally established fact that the rate of unfolding is driven by membrane tension.

The algorithm that defines D^A_{mem} is as follows:

1) As illustrated in Figure 2C, at the beginning stages of spreading a cell simply flattens from a spherical shape in suspension, and the increase in membrane tension is very small during this phase. In general, using (2.17), we can calculate a membrane unfolding strain rate that results in a prescribed rate of increase of membrane tension. For time $t < 0.7$ min D^A_{mem} is calculated so that the increase rate of the membrane tension is given by

$$\dot{\sigma}_{mem} = g_{mem} t, \tag{2.18}$$

where g_{mem} is the early-stage membrane tension increase rate. We chose the transition time value of $t = 0.7$ min by comparing cell spread areas to experimental results. Furthermore, experimental work indicates that it takes approximately one minute for nascent adhesions to form and stabilize [63]. Our choice of transition time is consistent with this time scale. The total FA complex that is present in the cell at time $t = 0.7$ min is stored and used in a later part of the algorithm. This stored value of ϕ^{TOT} at time $t = 0.7$ is referred to as ϕ^{TOT}_{ref}.

2) For $t \geq 0.7$ min, we use (2.17) in a novel way recognizing that unfolding, as represented in our model by D^A_{mem}, is tension-driven, FA-dependent and reduces that rate of membrane tension. Consequently, we first specify a rate of membrane tension that is reduced by an amount proportional to the total FA complex:

$$\dot{\sigma}^{D^A}_{mem} = e^{-k_\phi f(\phi^{TOT})} \dot{\sigma}_{mem}(t) \tag{2.19}$$

where

$$f(\phi^{TOT}) = \frac{\phi^{TOT}(t) - \phi^{TOT}_{ref}}{\phi^{TOT}_{max} - \phi^{TOT}_{ref}} \tag{2.20}$$

In (2.20), ϕ^{TOT}_{max} is the maximum possible value of total FA complex in the cell. (Note: it is equal to N_{max} used in (2.12)). The function (2.20) measures the change in the total amount of FA complex once unfolding is activated relative to the maximum change in total FA complex possible. By specifying the intermediate rate of change of membrane tension in this manner, we are incorporating the interaction between membrane unfolding and adhesions. We note that (2.19), and in fact, this entire algorithm, should be considered as a part of the constitutive description of the problem in the same manner as the specification of D^A_{mem} directly would be part of the constitutive description.

3) We now use (2.17) to solve for the active rate of membrane deformation, D^A_{mem}, that would result in the membrane tension rate defined in (2.19). For the purposes of the next step of the algorithm, we refer to the resulting value of D^A_{mem} as $\overline{D}^A_{mem}$.

4) Finally, to model the depletion of membrane reserves with time, we compute the active rate of membrane deformation used in time step $t + \Delta t$ according to

$$D^A_{mem}(t + \Delta t) = \overline{D}^A_{mem} e^{-d_m(t-0.7)} \tag{2.21}$$

where d_m is the membrane reserves decay parameter. This active rate of deformation is then used at the next time step to determine all mechanical and biochemical fields for which we are solving.

A more detailed description of this algorithm is given in Eqs (26)–(29) of the supplement.

All parameter values used in the Unfold model are in Table S4 of the supplementary material. This model is presented in this work for the first time and, to our knowledge, there are no experimental results that provide the parameter values for the Unfold model. As a result, the majority of the parameter

values used in the Unfold model are defined here for the first time. We have chosen a set of parameters that allow us to show that the membrane unfolding process described is a feasible way to explain the large cell spread areas observed in experiments.

2.6. Myosin contractility model

Myosin-induced cellular contractility is critical to cell motility [64, 65] and has also been shown to play a role in spreading [18]. Several models that include myosin contractility in the context of a model of the whole cell typically track the activation, degradation and transport of myosin and incorporate contractility by specifying an active force [30, 41, 58, 66, 67]. In the Contract model we take a more simplified approach by assuming that the rate of contraction is constant and use an additive decomposition of the deformation gradient approach similar to that used in Section 2.5 to model membrane unfolding. Specifically, we assume that the rate of deformation of the actin network is decomposed into a passive part, $\dot{\varepsilon}^p_{rr}$, and contractile part, $D^{contract}$, such that

$$\dot{\varepsilon}_{rr} = \frac{\partial v_c}{\partial r} = \dot{\varepsilon}^p_{rr} + D^{contract} \tag{2.22}$$

As described for the active deformation of the membrane, we assume that the contractile part of the rate of deformation is locally stress-free and all stresses depend only on the passive component. Under this assumption, (2.4) can be rewritten as

$$\sigma_r - K\Big(\frac{\partial v_c}{\partial r} - D^{contract}\Big) = 0 \tag{2.23}$$

(Recall that in the simulations described here we set the parameter λ from (2.4) to zero.) While it is possible to also prescribe an active rate of contraction in the angular direction, in the work here, we assume that contraction acts solely in the radial direction, which amounts to anisotropic contraction. Since contraction does not occur in the lamellipodium, which is the region closest to the cell periphery [68], we also assume that this active rate of contraction acts from the cell center to a distance 2 μm from the cell periphery and is constant.

Myosin-based contraction leads to increased intracellular tension, which is associated with the assembly and strengthening of focal FAs [31, 69]. To account for this in the Contract model, we add an additional term to the degradation rate for the FA complex that is dependent on intracellular tension making the evolution equation for ϕ

$$\frac{\partial \phi}{\partial t} \;=\; D\nabla^2\phi \;+\; k^0_{on}(N_{max} - \phi^{TOT})(\phi_{max} - \phi) \;-\; k^0_{off}e^{-k_a|f_{attach}|}\cdot e^{-k_\sigma h(\sigma_r)}\phi \tag{2.24}$$

where k_σ is the intracellular stress feedback parameter, and $h(\sigma_r)$ is a function whose value is determined by whether the intracellular stress is tensile ($\sigma_r > 0$) or compressive ($\sigma_r < 0$), such that

$$h(\sigma_r) = \begin{cases} \sigma_r & \sigma_r > 0 \\ 0 & \sigma_r < 0 \end{cases} \tag{2.25}$$

All parameter values used in the Contract model are in Table S5 of the supplementary material.

2.7. Model parameters and computational approach

The system-level model presented here requires the specification of several parameters found in Tables S1–S5 of the supplement. These tables also include references to publications providing these parameters whenever it is possible. We would like to note that the parameters for which there is no data in the literature have been selected after a thorough investigation of possible values and the effects of these values on the results. In this investigation, our goal was not to perform a sensitivity analysis, but rather to show that a set of parameter values exist that make the model feasible. We do this by comparing aspects of the simulation results to experimental data. Specific cases of these comparisons are described in the Results section. In the supplement, we also further comment on some of the parameter choices that were used in the model. In addition, we detail the computational implementation in Section 3 of the supplementary material.

3. Results

For all models discussed here the sensitivity of the cell spread area is presented as a relative difference, expressed in percentages, between the spread area for the softest (2.5 kPa) and stiffest (100 kPa) substrate that we consider. This percent increase is calculated as the substrate Young's modulus increases from 2.5 to 100 kPa relative to the spread area at 2.5 kPa. Also, in all cases the equilibrium cell spread area is calculated at time $t = 30$ min, at which point the cell spread area has plateaued or its rate of increase has significantly slowed down.

3.1. MM model results – Purely mechanical interactions contribute only slightly to mechanosensitive cell spreading due to membrane tension

The MM model accounts for purely mechanical interactions between the cell and substrate and spreading is driven by a constant polymerization speed, v_{poly}. Figure 3A shows that equilibrium cell spread areas are only slightly sensitive to the substrate Young's modulus and do increase with substrate stiffness, following the general trend of experimental results. The sensitivity of the cell spread area to substrate stiffness is only 2.5%.

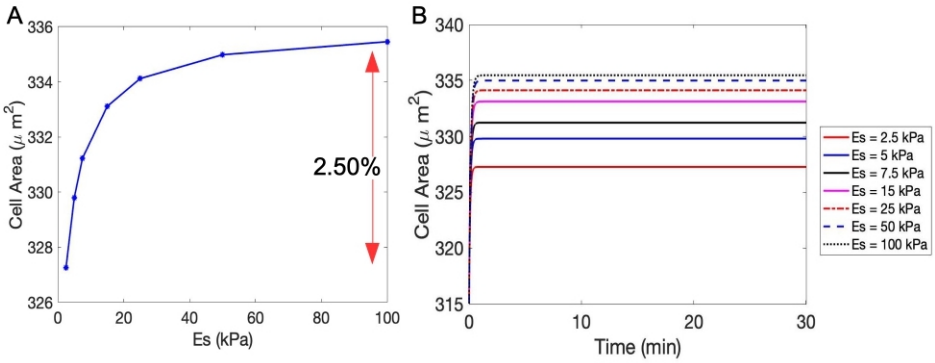

Figure 3. Cell area evolution for MM model and dependence on substrate Young's modulus. (A) Equilibrium cell area dependence on substrate Young's modulus. (B) Time evolution of cell area for different substrate stiffnesses.

In the MM model, cell spreading is limited by the stiffness of the membrane. The force from actin polymerization is quickly balanced by the force due to stretch in the membrane causing the cell area to plateau (Figure 3B). The slight increase in cell spread area on stiffer substrates can be attributed to the mechanical interactions of the actin with the substrate. To justify it, we recall that the radial velocity of the cell periphery, v_{periph}, is the sum of the polymerization velocity and the actin retrograde flow velocity: $v_{periph} = v_{poly} + v_c$. As substrate stiffness increases, actin retrograde flow speed decreases due to the frictional interaction with the substrate and the net spreading velocity is higher, also leading to a slightly higher spread area on stiffer substrates.

3.2. FA model results – Total FA amounts depend on substrate stiffness

In the FA model the mechanical interactions from the MM model are augmented with an attachment-traction-dependent FA evolution given by (2.12) and an FA complex-dependent interaction with the substrate given by (2.13). The inclusion of these mechanisms in the FA model allows us to capture the sensitivity of the total FA complex amount, ϕ^{TOT}, to substrate stiffness that is in qualitative agreement with experimental measures of total active integrin dependence on substrate stiffness Figure 4A [4]. Total FA complex amounts are calculated at time $t = 30$ min, by which time an equilibrium level in ϕ^{TOT} is reached. We note that in the FA model we are not aiming for a quantitative comparison to experimental results, but rather a qualitative comparison. The experimental results in the right panel of Figure 4A are obtained from a western blot assay, which is only able to quantify an amount of protein present in cells relative to a reference quantity. For this reason, ϕ is measured in arbitrary units (a.u.), which does not allow for a quantitative comparison. Thus, in Figure 4A we are illustrating that the general trend in both the simulations and experiments is that total FA complex amounts increase with substrate stiffness. This trend is also supported by the experimental observation that the size of individual FAs also increase with substrate stiffness [70].

The inclusion of attachment-traction-dependent FA evolution enhances the sensitivity of the cell spread area to substrate stiffness; the equilibrium cell spread area increases by 16.66% as the substrate Young's modulus increases from 2.5 kPa to 100 kPa (Figure 4B). The primary mechanism behind this slight enhancement in cell spread area is a stronger attachment to the substrate, which slows down retrograde flow allowing the velocity at the cell periphery to increase. Figure 4C shows a comparison of the time evolution of retrograde flow speeds at the cell periphery for the MM model and FA model for a soft ($E_s = 2.5$ kPa) and stiff ($E_s = 100$ kPa) substrate. In the MM model, the retrograde flow speeds slightly decrease for a cell spreading on a stiff substrate (grey curves, solid and dashed). However, in the FA model, there is a larger decrease in the retrograde flow speed on a stiff substrate compared to a soft substrate (black curves, solid and dashed), leading to larger velocities at the cell periphery and larger cell spread areas. In essence, the FA model captures the clutch mechanism that describes how active engagement of a cell with the substrate through activated integrins results in the outward motion of the cell periphery [71].

The mechanisms included in the FA model also enhance the localization of traction stresses to the cell periphery (Figure S2A,B). The localization of traction stresses to the cell periphery serves as one key mechanism to slow down retrograde flow in the entire cell interior. In the MM model, traction stresses are small, in part because cellular spread areas are also small. In the FA model, maximum traction stresses increase approximately 4-fold relative to the MM model (compare maximum stresses in Figure S2A,B). However, because cell spread areas that arise from the FA model remain smaller than

those observed experimentally, our computed traction stresses are also smaller than those measured experimentally (Figure S2C) [72]. However, the spatial localization of the traction stresses compares qualitatively to experimental results, and we also note that in both the MM model and FA model, the traction stresses increase with substrate stiffness, which is also seen experimentally.

It is clear that additional biophysical and biochemical mechanisms need to be accounted for to explain the substantially large increases in cell spread area on stiff substrates that is seen in experiments. We also note that the subsequent mechanisms that we layer in the model focus on ways in which cells respond to the FA model. However, other than the Contract model, these additional mechanisms do not feedback to the FA model. These new mechanisms do not significantly alter the total FA amounts for a given substrate stiffness, and therefore we will not focus on the FA sensitivity to substrate stiffness henceforth.

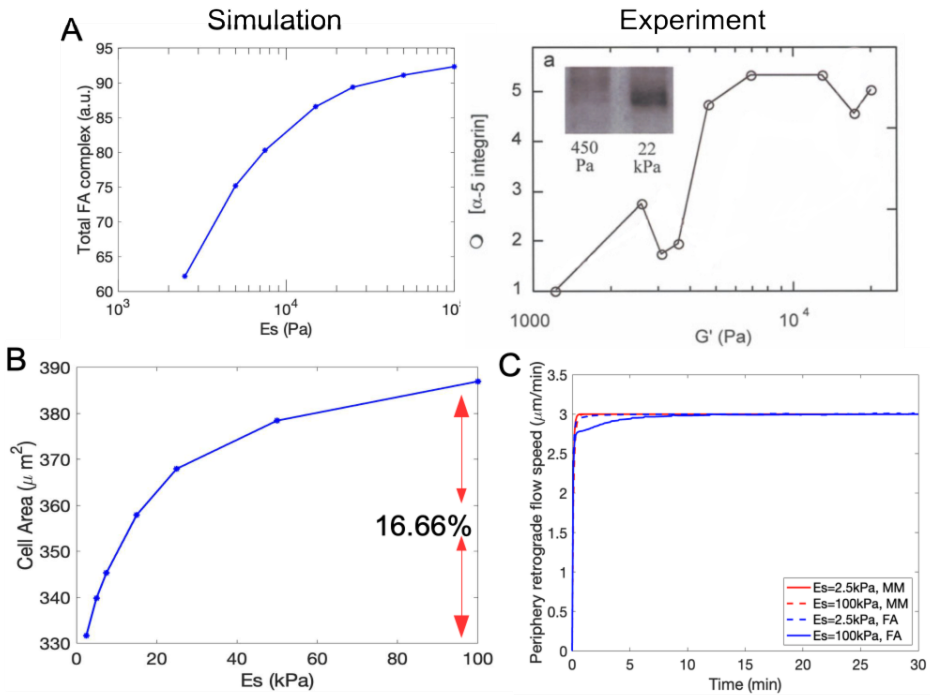

Figure 4. FA model – dependence of total FA complex and cell area on substrate Young's modulus. (A) Qualitative comparison between numerical simulations and experimental results of the dependence of total FA complex (ϕ^{TOT}) on substrate stiffness. Experimental results in the right top panel show amounts of activated integrin relative to the active integrin amount at a shear modulus, G', of approximately 1000 Pa [4] (reproduced with permission). The relationship between the shear modulus G' and substrate Young's modulus E_s is given by $G' = E_s/(2(1+\nu_p))$. (B) Equilibrium cell area dependence on substrate Young's modulus. (C) A comparison of time evolution of retrograde flow speeds at cell periphery for the MM model and FA model on soft (2.5 kPa) and stiff (100 kPa) substrates.

3.3. *Poly model results – Adding FA-dependent actin polymerization is not sufficient to recapitulate cell spread area dependence on substrate stiffness*

The FA-complex polymerization speed (see (2.14)) in the Poly model aims to enhance the sensitivity of the cell spread area to substrate stiffness by strengthening the coupling between the FA complex and components that increase the rate of cell spreading, namely the polymerization speed. To test that our parameter choices for the FA-dependent polymerization velocity are appropriate, we compare retrograde flow speeds predicted by our model to experimentally measured retrograde speeds in motile growth cones [73]. We compare retrograde flow speeds because the predicted retrograde flow speeds in Figure 5A are measured at time $t = 30$ min, when the cell spread area has reached equilibrium. At this point, the actin retrograde flow speeds are balanced by the polymerization speed. Hence a comparison of predicted and experimental retrograde flow speeds is an indicator that polymerization velocities are modeled appropriately. Actomyosin contractions are known to affect retrograde speeds [74], and we acknowledge that we do not include myosin contractility in the Poly model. However, we do measure how our model of myosin contractility affects retrograde flow below in the Contract model results and find that, within the context of our modeling approach, contractility does increase retrograde flow rates, but not significantly (see Figure S8 in supplement). Our computed retrograde flow speed dependence on substrate stiffness compares relatively well to experimental results, indicating that the polymerization velocity is modeled using a reasonable set of parameters given the model equation that we employ.

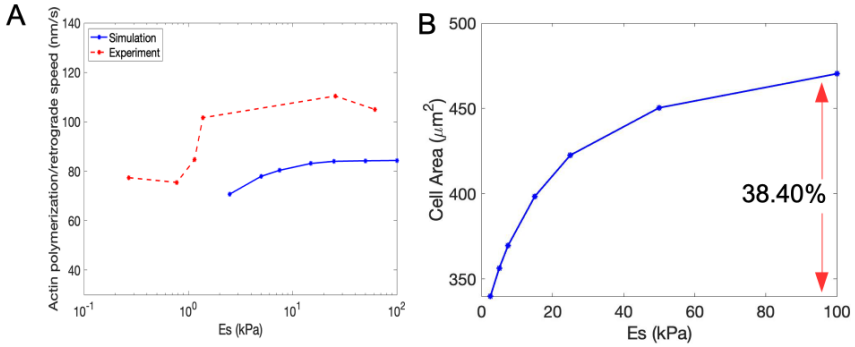

Figure 5. Poly model – Dependence of cell area and polymerization speed on substrate Young's modulus. (A) Comparison between numerical prediction and experimental results of the dependence of retrograde flow speed on the substrate Young's modulus. Retrograde flow speeds are computed at $t = 30$ min, i.e. when equilibrium cell spread area is reached and actin retrograde flow speeds are equal to polymerization speeds. Experimental results are reproduced from [73] by using the ImageJ software [75]. (B) Equilibrium cell area dependence on substrate Young's modulus for Poly model.

The effect of adding an FA-complex dependent polymerization velocity in the Poly model further enhances the sensitivity of the. cell spread area to substrate stiffness. In the Poly model, the equilibrium cell spread area increases by 38.40% as the substrate Young's modulus increases from 2.5 kPa to 100 kPa (Figure 5B). As noted earlier, the velocity of the cell periphery, which determines the cell spread area, is the sum of the polymerization velocity and the retrograde flow velocity. The mechanical

process that allows for an increased difference in cell spread areas in the Poly model is mediated by increasing the polymerization speed (oriented toward the cell periphery) relative to the retrograde flow speed (oriented toward the cell interior) for an increased amount of time. While the inclusion of this mechanism increases the cell spread area, it is still not comparable to experimental observations. Hence, we explore an additional mechanism in the following section.

3.4. Unfold model results – Tension-dependent membrane unfolding is critical for obtaining significant enhancement in cell spread area on stiff substrates

In the Unfold model we account for membrane unfolding and exocytosis of membrane reserves as an active rate of membrane deformation, which is defined algorithmically (see Section 2.5). Including the effects of membrane unfolding / exocytosis on top of the existing mechanisms described in the previous sections results in a significant increase in cell spread areas that compares to experimentally observed results. This suggests that we potentially have the minimal set of mechanisms in our model to account for the sensitivity of the cell spread area to the substrate Young's modulus. In the Unfold model, the cell spread area increases by 267.62% as the substrate Young's modulus increases from 2.5 kPa to 100 kPa (see Figure 6A, right panel). As will be discussed more in the next section, in the Unfold model it is specifically the combination of an FA-dependent actin polymerization velocity and membrane unfolding that allows for such large differences in cell spread area in response to substrate stiffness.

We note here that the experimental results show that membrane tension decreases during spreading [23, 27], whereas the membrane tension in our simulations increases with spread area (Figure S3, bottom row). This is a deficiency of the model. However, for the large spread areas that we obtain in our model, the membrane tension would be significantly higher if membrane unfolding was not included. In the Discussion, we name some possible modifications that could be investigated as a way to mitigate this problem. Each of them constitute an expansion of our approach warranted in a separate investigation.

Experimentally measured membrane tether forces range from 7 pN to 70 pN, depending on cell type, with most values ranging from 20–40 pN [76]. The tension in a cell membrane is approximated by squaring the tether force [24], which leads to membrane tensions in experimental work ranging from 49 pN to 4900 pN, with most values being between 400–1600 pN. We also note that an increase in membrane tension on stiffer substrates has been observed experimentally [77]. Therefore, despite the qualitative difference between the membrane tension resulting from our model and experimental work, our computed membrane tension values at equilibrium (time $t = 30$ min) are in line with the membrane tension measured experimentally.

Our model predicts an increased membrane growth on stiffer substrates (Figure S4A). Furthermore, during spreading the membrane area increases by at least 20% due to the unfolding of folded membrane regions [22] . These experimentally measured increases are in line with what we found computationally (Figure S4A). The results in Figure S4A were obtained as follows: taking the membrane to be a strip of height $h = 1$ μm along the cell periphery, the original membrane area in our calculations is 62.83 μm^2. The membrane area added is approximately 12–20 μm^2, depending on the substrate Young's modulus, which is 19–32% of the original area. The membrane area added at time t was calculated by using the integral $\int_0^t 2\pi r(\tau) h D^A_{mem}(\tau)\, d\tau$, where $r(t)$ is the cell radius at time t. While, locally, the sensitivity of unfolding strain rates to substrate stiffness is small (Figure S4B), these small changes manifest as

increasingly larger differences in growth of the membrane area, which contributes to the overall growth in cell spread areas.

3.5. Alternate combination of mechanisms – Membrane unfolding and FA-dependent actin polymerization work synergistically to enhance cell spread area sensitivity to substrate stiffness

Figure 6A illustrates the increase in cell spread area if membrane unfolding is added to the FA model while the polymerization speed is kept constant, which results in the Constant Poly - Unfold model. Because the ability to sense the mechanical properties of the substrate is critical to spreading, we use the FA model, and not the MM model, as a starting point. In the Constant Poly - Unfold model, we use a constant polymerization speed ($v_{poly} = 3\,\mu$m/min), and the cell spread area increases by 81.40%. This is compared to the Poly model (no unfolding, FA-dependent polymerization speed), in which the cell spread area increases by 38.4%, and the Unfold model (includes both unfolding and FA-dependent polymerization speed), in which the cell spread area increases by 267.62%. These results indicate that, while membrane unfolding seems to be the most important component in achieving enhanced cell spread areas on stiffer substrates, the combination of membrane unfolding and FA-dependent actin polymerization results in a nonlinear amplification that leads to the large cell spread area sensitivity that is observed experimentally.

To better understand how the Poly model, Const Poly - Unfold model and Unfold model affect cell spread areas, in Figure 6B we compare actin polymerization speeds, actin retrograde flow speeds at the cell periphery and the peripheral velocity for these three models spreading on a soft (2.5 kPa) and stiff (100 kPa) substrate. For the purpose of subsequent discussion, we subdivide the simulation time of 30 min into three temporal phases: Phase ① is approximately 0–3 min, Phase ② of approximately 3–15 min, and Phase ③ of approximately 15–30 minutes. We note that [18] also subdivides the temporal evolution of cell spreading into three phases of similar lengths and with similar behaviors.

In the Const Poly - Unfold model, the polymerization speed is fixed, while, due to a large initial burst of membrane unfolding, retrograde flow speeds are small in early times. This causes the peripheral velocity, v_{periph}, to be initially large (note Phase ① in Figure 6B). The peripheral velocity then rapidly decreases as the retrograde flow speed approaches the polymerization speed (during times in phases marked by ② and ③). We note that in the Const Poly - Unfold model, the peak values of v_{periph} for 2.5 kPa and 100 kPa are comparable, but the rate of decay is slower on stiffer substrates in Phase ②, leading to larger cell spread areas.

In the Poly model, the polymerization speed is larger on a stiff substrate. Due to a lack of membrane unfolding, the retrograde flow speeds rapidly reach values equal to the actin polymerization speeds, and v_{periph} remains small leading to smaller cell spread areas overall.

In the Unfold model, the polymerization speed is also larger on a stiff substrate. However, retrograde flow speeds to do not increase as quickly as they do for the Poly model, which leads to a larger v_{periph} in Phase ①. The membrane unfolding also decreases the decay rate of v_{periph} on stiff substrates, in particular, in Phase ②, which leads to large spread areas. Time evolution of the polymerization speeds, retrograde flow speeds and peripheral velocities for all substrate Young's moduli that we consider are illustrated in Figure S3.

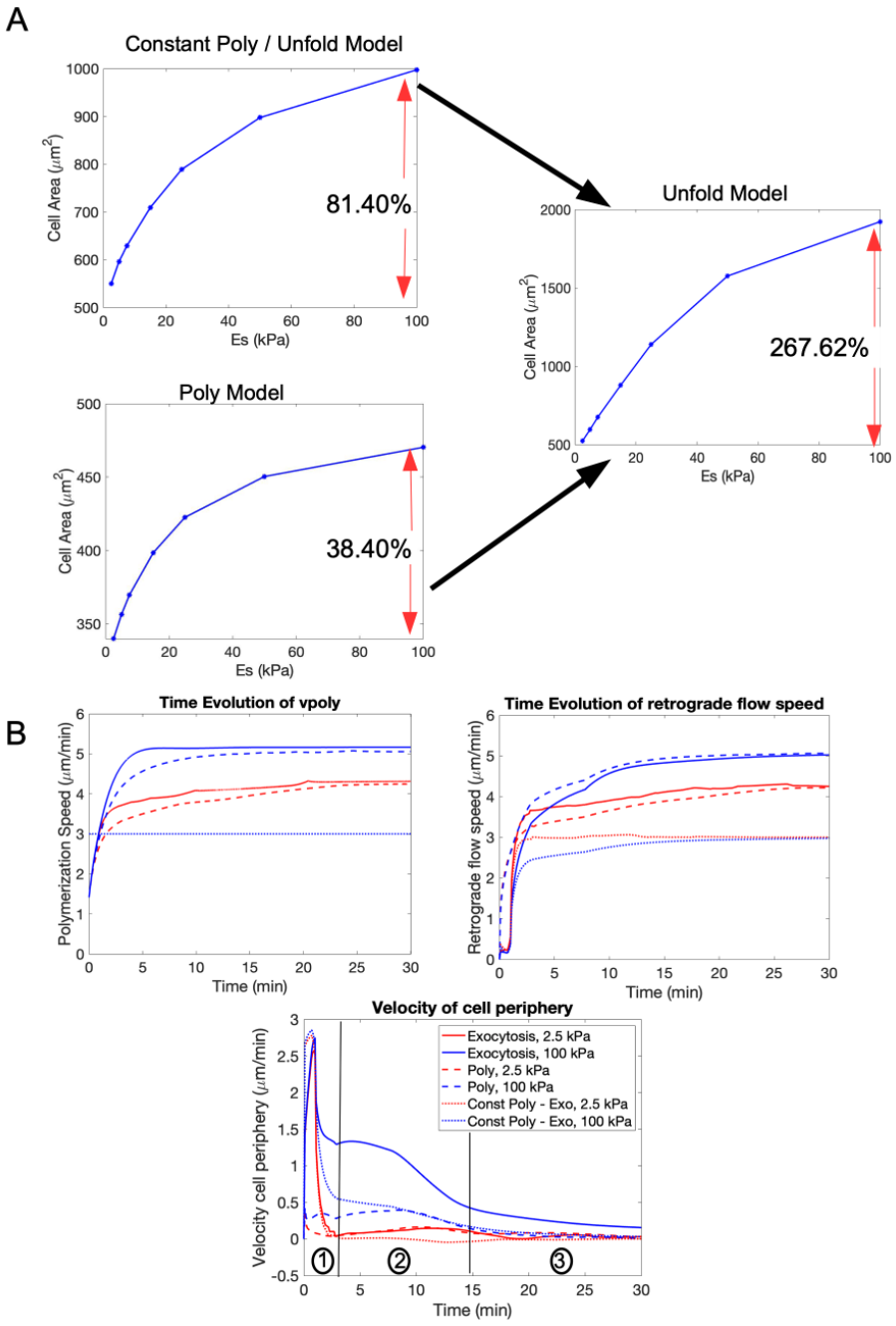

Figure 6. Comparison of the effects of membrane unfolding and adhesion-dependent polymerization speed on cell spread area. (A) Cell spread area dependence on substrate Young's modulus for the Const Poly - Unfold model (top left), the Poly model (bottom left), and the Unfold model (right). (B) Actin polymerization speed (top, left), retrograde flow speed at cell periphery (top, right), and velocity of cell periphery (bottom) for the Const Poly - Unfold model (dotted lines), the Poly model (dashed lines) and the Unfold model (solid lines). We compare each of these on a soft ($E_s = 2.5\,kPa$, red) and stiff ($E_s = 100\,kPa$, blue) substrate.

3.6. Contract model results - Myosin contractility does not contribute to mechanosensitivity in cell spreading

The Contract model introduces myosin-induced contractility and catch-bond feedback from intracellular tensile stress to FA activation. Our results show that the addition of contraction and tensile stress feedback to FA evolution does not significantly the affect sensitivity of cell spread areas to substrate stiffness. In Figure 7A, we show that, when contractility is included, the cell spread area increases by 203.96% as the substrate stiffness increases from 2.5 kPa to 100 kPa. Because the Contract model contains a full set of fundamental biophysical mechanisms that have experimentally been shown to affect cell spreading, in Figure 7B we compare the time evolution of cell spread areas on different substrates to the temporal evolution of the spread area measured experimentally [4]. Our model compares well to experimental results.

When one includes contractility and tensile stress feedback to FA evolution and adds unfolding to the FA model while keeping polymerization speeds constant (such as is done in Section 3.5), the same general trend in cell area dependence on substrate stiffness is observed as when contractility is not included (See Figure S5). Namely, the Poly model plus contraction leads to a cell spread area increase of 37.88%, and the Const Poly - Unfold model plus contraction results in an area increase of 60.96%. Compare this to the results in Figure 6A. Therefore, the addition of myosin-based contraction seems to slightly decrease cell spread areas and sensitivity to the substrate stiffness. This is not surprising given that mechanical contraction generates movement that acts in the direction opposite of actin polymerization and increases retrograde flow speeds at the cell periphery (see Figure S6). In addition, we note that the value of the intracellular stress feedback parameter k_σ has little impact on spread areas obtained via the Contract model; when this parameter is increased from $k_\sigma = 10$ $(\text{Pa})^{-1}$ (Figure 7) to $k_\sigma = 100$ $(\text{Pa})^{-1}$ (Figure S7A), the cell spread increase is 193.44%.

Since contraction does not significantly affect cell spread area, what is a potential role of contractility in cell spreading? To investigate this we compared the radial component of the Cauchy stress tensor for the Unfold model and the Contract model (Figure 7C). The top row of Figure 7C shows that the radial stress in the Unfold model is compressive (i.e., stress values are < 0) for both the softest (2.5 kPa) and stiffest (100 kPa) substrates we consider. On the other hand, the second row of Figure 7C illustrates that when contraction is present in the model, the stresses in the cell interior are tensile (stress values are > 0). Therefore, these results indicate that a primary role of myosin contractility is to keep the interior of the cell in a state of tension. The total amount of FA complex in the cell is limited to N_{max}, and there is little difference in the sensitivity of the total amount of FA complex to substrates stiffness whether or not contractility is included (Figure S7C). The interior tension causes both a slight increase in retrograde flow speed and a commensurate decrease in peripheral velocity causing the cell spread area to decrease in the presence of contractility and greater values of k_σ.

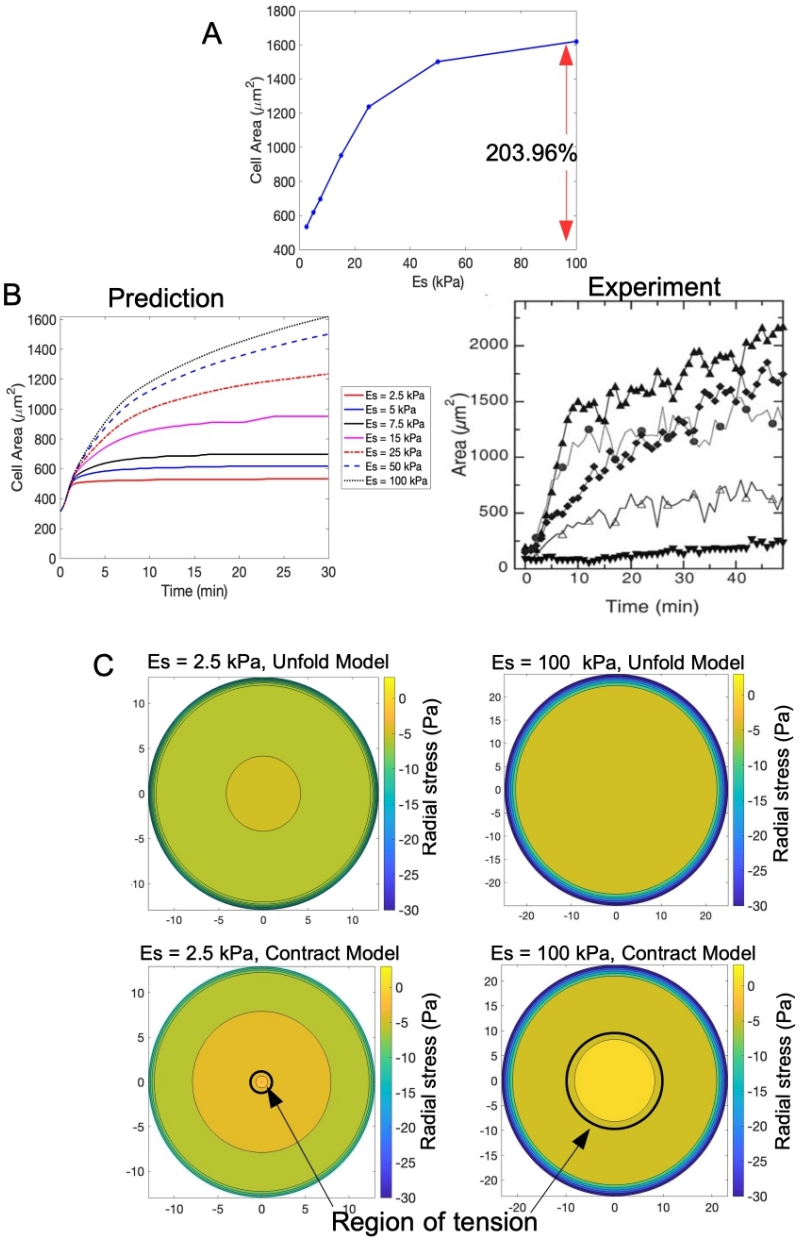

Figure 7. Contract model – Effects of substrate Young's modulus on cell spread area and intracellular stress for $k_\sigma = 10$ (Pa)$^{-1}$: (A) Dependence of equilibrium cell spread area on substrate Young's modulus. (B) A comparison between numerical prediction and experimental results in terms of the time evolution of cell area for various substrate stiffnesses. Substrate stiffnesses considered in the experimental results are from > 0.18 kPa to 55 kPa. Experimental results are from [4] (reproduced with permission). (C) A comparison of radial stresses (σ_{rr}) at time $t = 30$ min for $E_s = 2.5$ kPa and $E_s = 100$ kPa for the Unfold model (no contraction) and the Contract model. Black circles mark regions of intracellular tension ($\sigma_{rr} > 0$).

4. Discussion

Starting off with a mechanistic model of a spreading cell interacting with a deformable substrate, we have developed a system level model of cell spreading that includes various combinations of key mechanisms that are known to be present in spreading cells: 1) traction-dependent growth of FAs, 2) active integrin-dependent actin polymerization, 3) tension-dependent membrane unfolding/exocytosis and 4) myosin-based contractility. Combining these mechanisms in alternate ways enables us to determine the effect that these combinations have on the sensitivity of cell spread areas to substrate stiffness.

The main contribution of this work is that the mechanism that has the dominant effect on increasing cell spread areas on stiffer substrates is membrane unfolding. When layering membrane unfolding on the FA model (to create the Constant Poly / Unfolding model), we see an 81.4% increase in cell spread areas as the substrate Young's modulus increases from 2.5 kPa to 100 kPa. However, we find that the combination of FA-dependent polymerization and membrane unfolding is required to obtain the 200–300% increase in cell spread areas experimentally observed as substrate stiffness increases from approximately 1 kPa to approximately 100 kPa. Specifically, layering FA-dependent polymerization on the FA model (to create the Poly model) results in an 38.4% increase in cell spread area. However, when both FA-dependent polymerization and membrane unfolding are combined together (Unfold model), their effects are amplified nonlinearly due to a synergistic coupling between two mechanisms, which causes a simultaneous increase in polymerization speed and decrease in retrograde flow speed, to obtain a 267.62% increase in cell spread area. This finding, along with the algorithm to determine membrane unfolding rate, is the novel contribution of the present work. The detailed mechanism behind this synergistic coupling is discussed later from the perspective of key determinants influencing cell spread area.

The modeling approach employed herein also provides insight into other mechanisms involved in mechanosensitive cell spreading. Our results are consistent with experimental work, which indicates that an increase in myosin II activity (leading to increased contractility) slows down the rate of cell spreading and leads to smaller cell spread areas [74, 78]. The maximum cell spread area on a substrate with a Young's modulus of 100 kPa is 1922 μm^2 in the Unfold model, whereas it decreases to 1629 μm^2 in the Contract model. Similarly, the percent increase in cell spread area as substrate stiffness increases from 2.5 kPa to 100 kPa is 267.62% in the Unfold model and 203.96% in the Contract model. We find that the main role of myosin-based contractility is to keep portions of the cell interior in a state of tension (vs. compression). It has been shown that stress fibers usually exist in the cell in a tensile state [79, 80], and tension has been found to play a critical role in the mechanotransduction processes such tumor progression and polarization during motility [81–83]. Consistent with experimental work [84], we find that retrograde flow speeds at the cell periphery are larger for the Contract model than when contraction is not present (Figure S6). This increase in retrograde flow speed at the cell periphery causes decreased peripheral velocities during spreading, which provides an explanation of the decrease in cell spread areas observed in the Contract model.

The main determinant of the cell spread area is the velocity of the cell periphery and the rate at which this velocity decays to zero. Thus, a remaining question is how does including FA-dependent actin polymerization and membrane unfolding affect the balance of retrograde flow speed and polymerization speed at the cell periphery? In the Poly model, an increase in the total FA complex with substrate stiffness increases the polymerization speed on stiffer substrates, and this alone is enough to

obtain larger peripheral velocities on stiffer substrates. However, without membrane unfolding there is no large burst in peripheral cell velocities at early times (Phase ① in Figure 6B), and the peripheral velocities remain small (at peak values no larger than 0.5 μm/min) and decay to zero. In both the Constant Poly- Unfold model and the Unfold model, there is an initial burst in membrane unfolding (see Figure S4), which significantly slows down retrograde flow speeds relative to the polymerization speed in Phase ① and leads to a large burst in the peripheral cell velocity in this phase.

Membrane unfolding also affects the rate at which the velocity at the cell periphery decreases as the cell reaches a steady state spread area. Through the dependence of the active rate of membrane deformation on the total FA complex, the model results in an increase in the membrane unfolding rate for larger substrate stiffnesses. In terms of the relationship between the polymerization speed and retrograde flow speed, larger rates of membrane unfolding slow down retrograde flow, thereby increasing the velocity of the cell periphery in Phase ②. This results in a substrate stiffness dependent variation in the rate of decay of the velocity at the cell periphery (see Phase ② in Figure 6B). Namely, on stiff substrates the velocity of the cell periphery decreases more slowly than on soft substrates, and this further enhances the differences of cell spread areas on substrates of different stiffnesses. Overall, membrane unfolding affects the temporal evolution of the retrograde flow speed, and the final cell area is highly dependent on the dynamics of this evolution. The addition of FA-dependent actin polymerization along with membrane unfolding works to enhance the differences between the polymerization and retrograde flow speeds, leading to a more significant increase in cell spread areas. This in essence results in the previously described synergistic coupling between FA-dependent polymerization and membrane unfolding resulting in a nonlinear amplification of the cell spread area.

The cell area evolution behavior in phases labeled ①, ②, ③ in Figure 6B are consistent with the experimental results [18]. In [18], the authors describe that the dynamics of cell spreading from Phase P1 to Phase P2 and to a steady-state spread area, and they attribute it to an evolving balance of protrusive and retractive events. Phase P1, during which cell spreading is rapid, corresponds, in our model, to Phase ①. While our model does not consider periodic protrusion and retraction events explicitly, we do find that, in Phase ①, the velocity of cell spreading is controlled primarily by a large polymerization speed relative to retrograde flow speed. This large difference between these two speeds is attributed to rapid membrane unfolding in Phase ①. As the rate of membrane unfolding slows down, the retrograde flow speeds increase and approach the value of the polymerization speed. This occurs in Phase ②, which corresponds to Phase P2 of cell spreading in [18], during which cell spread rates decrease. Experimentally, this corresponds to an increase in the frequency of retractive events. Finally, during the last phase of cell spreading, the frequency of protrusive and retractive events are in balance, and the cell area reaches a steady state. In our work, this occurs in Phase ③, in which the polymerization speeds and retrograde flow speeds are close to being equal. In Phase ③, membrane unfolding has ceased due to depleted membrane reserves. This comparison to the spreading dynamics described in [18] also serves as additional verification that the overall features of the model are realistic.

An additional noteworthy aspect of the modeling effort described herein is that the resulting qualitative agreement with experiments was achieved by employing parameters resulting from independent past investigations of which we were aware. Although the new constants we need here were adjusted to reproduce some of the features of cell spreading seen in experiments, we believe that extensive use of independent research by other investigators is a factor adding to the plausibility of the mechanisms we consider, in particular the new Unfold model we advance in this work.

In addition to furthering the understanding of how various mechanisms affect the temporal evolution of processes required for mechanosensitivity during cell spreading, the mechanisms described in this work also serve to reinforce and expand on the role of coupling between local signals with large-scale mechanosensing of substrate stiffness, as highlighted by Trichet et al [85]. In their work, it is observed that the growth of local FAs depends not only on the attachment strength at the location of an FA but also on global deformations of the cytoskeleton in areas away from FA locations. Specifically they highlight the role of traction stresses localized to FAs that induce larger scale reorganization of the cytoskeleton and reorientation of stress fibers which then reinforce the coupling with the susbtrate. Our work builds on this larger scale mechanosensing by highlighting two additional mechanisms: i) local FA-induced enhancement in polymerization at the cell periphery, (ii) an FA-controlled membrane unfolding. Both occur at scales larger and farther from where the FAs are localized. This indirectly accounts for the underlying biochemical pathway that transduces signals across space to create larger multiplicative forces leading to enhanced cell spreading. In addition, localized cell-substrate traction stresses enhance cell spreading by controlling global values of retrograde flow speeds. This retrograde flow in turn serves to modulate the local attachments which, in our model, occurs by the reduction in the detachment rates of the FAs. These groups of mechanisms together serve to bring in a much more nuanced picture of the coupling between the local and large-scale mechanisms highlighted in [85], while simultaneously drawing attention to a previously less explored role of tension and FA induced membrane unfolding to accelerate cell spreading on stiffer substrates.

Cell spreading is a highly complicated process, and some drawbacks of this model are that we simplify the cell geometry, assume a homogeneous cell composition and simplify the descriptions of many inherently complex biomechanical interactions so that the model and resulting simulations are tractable. For the time intervals considered here, our assumption of homogenous material properties and axial symmetry are validated by the fact that, for most stages of cell spreading, many cell types remain unpolarized and retain a circular morphology. However, upon reaching their equilibrium cell area, the formation of stress fibers leads to possible cellular polarization [86]. Our model assumptions do not allow us to capture this late-stage polarization during spreading; a two-dimensional extension of our model would be necessary. Another drawback of the model is that it predicts an increase in membrane tension with the unfolding of membrane reserves, while experimental results show a decrease in tension in later stages of spreading [23, 27]. One can think of several ways of mitigating this issue. One modification would be to make membrane the material parameters deformation-dependent, which is typical for large deformation problems [87]. In fact, this is the approach used in [39]. An alternative modification is to change the way that the active rate of membrane deformation is defined. However, each modification presents its own set of difficulties if one is to account for all known biological processes involved in cell spreading in a consistent manner. We note, however, that without the addition of unfolding into the model, a large membrane tension would occur much sooner in the spreading process and would not allow for the prediction of cell spread areas that are comparable to experimental results.

Recent experimental advances are shedding light on new mechanisms that might be involved in cell spreading, such as volume control. In future work, we plan on using mathematical modeling and simulation to explore the effects of such newly emerging mechanisms. However, in aiming to capture the key components that are currently known to be required in spreading, we find a key takeaway from our work: the unfolding of the cell membrane potentially plays a critical role during spreading. To our knowledge, there is no experimental work that investigates the effect of knocking out membrane un-

folding or exocytosis ability on spreading. One of our aims in this work is to inspire such experimental investigations so that the biomechanical mechanisms involved in mechanosensitvity can continue to be unraveled.

Acknowledgments

The authors would like to thank Corning Inc. and the Center for Applied Mathematics at the University of St. Thomas for supporting this work. We also thank Prof. Henryk Stolarski for a careful reading of the manuscript.

Conflict of interest

The authors declare the following financial interests/personal relationships which may be considered as potential competing interests: Magdalena Stolarska reports that financial support was provided by Corning Incorporated. Aravind Rammohan reports employment with Corning Incorporated.

References

1. A. J. Engler, S. Sen, H. L. Sweeney, D. E. Discher, Matrix elasticity directs stem cell lineage specification, *Cell*, **126** (2006), 677–689. https://doi.org/10.1016/j.cell.2006.06.044
2. S. Li, N. F. Huang, S. Hsu, Mechanotransduction in endothelial cell migration, *J. Cell. Biochem.*, **96** (2005), 1110–1126. https://doi.org/10.1002/jcb.20614
3. F. Broders-Bondon, T. H. Nguyen Ho-Bouldoires, M. E. Fernandez-Sanchez, E. Farge, Mechanotransduction in tumor progression: the dark side of the force, *J. Cell Biol.*, **217** (2018), 1571–1587. https://doi.org/10.1083/jcb.201701039
4. T. Yeung, P. C. Georges, L. A. Flanagan, B. Marg, M. Ortiz, M. Funaki, et al., Effects of substrate stiffness on cell morphology, cytoskeletal structure, and adhesion, *Cell Motil. Cytoskeleton*, **60** (2005), 24–34. https://doi.org/10.1002/cm.20041
5. J. Solon, I. Levental, K. Sengupta, P. C. Georges, P. A. Janmey, Fibroblast adaptation and stiffness matching to soft elastic substrates, *Biophys. J.*, **93** (2007), 4453–4461. https://doi.org/10.1529/biophysj.106.101386
6. S. Y. Tee, J. Fu, C. S. Chen, P. A. Janmey, Cell shape and substrate rigidity both regulate cell stiffness, *Biophys. J.*, **100** (2011), L25–L27. https://doi.org/10.1016/j.bpj.2010.12.3744
7. G. Vertelov, E. Gutierrez, S. Lee, E. Ronan, A. Groisman, E. Tkachenko, Rigidity of silicone substrates controls cell spreading and stem cell differentiation, *Sci. Rep.*, **6** (2016), 1–6. https://doi.org/10.1038/srep33411
8. J. P. Califano, C. A. Reinhart-King, A balance of substrate mechanics and matrix chemistry regulates endothelial cell network assembly, *Cell. Mol. Bioeng.*, **1** (2008), 122–132. https://doi.org/10.1007/s12195-008-0022-x
9. C. A. Mullen, T. J. Vaughan, K. L. Billiar, L. M. McNamara, The effect of substrate stiffness, thickness, and cross-linking density on osteogenic cell behavior, *Biophys. J.*, **108** (2015), 1604–1612. https://doi.org/10.1016/j.bpj.2015.02.022

10. H. Wolfenson, B. Yang, M. P. Sheetz, Steps in mechanotransduction pathways that control cell morphology, *Annu. Rev. Physiol.*, **81** (2019), 585–605. https://doi.org/10.1146/annurev-physiol-021317-121245

11. S. Romero, C. Le Clainche, A. M. Gautreau, Actin polymerization downstream of integrins: signaling pathways and mechanotransduction, *Biochem. J.*, **477** (2020), 1–21. https://doi.org/10.1042/BCJ20170719

12. F. Kong, A. J. García, A. P. Mould, M. J. Humphries, C. Zhu, Demonstration of catch bonds between an integrin and its ligand, *J. Cell Biol.*, **185** (2009), 1275–1284. https://doi.org/10.1083/jcb.200810002

13. N. Strohmeyer, M. Bharadwaj, M. Costell, R. Fässler, D. J. Müller, Fibronectin-bound $\alpha 5\beta 1$ integrins sense load and signal to reinforce adhesion in less than a second, *Nat. Mater.*, **16** (2017), 1262–1270. https://doi.org/10.1038/nmat5023

14. S. Walcott, D. H. Kim, D. Wirtz, S. X. Sun, Nucleation and decay initiation are the stiffness-sensitive phases of focal adhesion maturation, *Biophys. J.*, **101** (2011), 2919–2928. https://doi.org/10.1016/j.bpj.2011.11.010

15. A. Elosegui-Artola, X. Trepat, P. Roca-Cusachs, Control of mechanotransduction by molecular clutch dynamics, *Trends Cell Biol.*, **28** (2018), 356–367. https://doi.org/10.1016/j.tcb.2018.01.008

16. J. D. Owen, P. J. Ruest, D. W. Fry, S. K. Hanks, Induced focal adhesion kinase (fak) expression in fak-null cells enhances cell spreading and migration requiring both auto-and activation loop phosphorylation sites and inhibits adhesion-dependent tyrosine phosphorylation of pyk2, *Mol. Cell. Biol.*, **19** (1999), 4806–4818. https://doi.org/10.1128/mcb.19.7.4806

17. E. A. Cavalcanti-Adam, T. Volberg, A. Micoulet, H. Kessler, B. Geiger, J. P. Spatz, Cell spreading and focal adhesion dynamics are regulated by spacing of integrin ligands, *Biophys. J.*, **92** (2007), 2964–2974. https://doi.org/10.1529/biophysj.106.089730

18. G. Giannone, B. J. Dubin-Thaler, H. G. Döbereiner, N. Kieffer, A. R. Bresnick, M. P. Sheetz, Periodic lamellipodial contractions correlate with rearward actin waves, *Cell*, **116** (2004), 431–443. https://doi.org/10.1016/S0092-8674(04)00058-3

19. H. Wolfenson, T. Iskratsch, M. P. Sheetz, Early events in cell spreading as a model for quantitative analysis of biomechanical events, *Biophys. J.*, **107** (2014), 2508–2514. https://doi.org/10.1016/j.bpj.2014.10.041

20. M. P. Sheetz, J. E. Sable, H. G. Döbereiner, Continuous membrane-cytoskeleton adhesion requires continuous accommodation to lipid and cytoskeleton dynamics, *Annu. Rev. Biophys. Biomol. Struct.*, **35** (2006), 417–434. https://doi.org/10.1146/annurev.biophys.35.040405.102017

21. D. Boal, *Mechanics of the Cell*, Cambridge University Press, 2012. https://doi.org/10.1017/CBO9781139022217

22. L. Figard, A. M. Sokac, A membrane reservoir at the cell surface: unfolding the plasma membrane to fuel cell shape change, *Bioarchitecture*, **4** (2014), 39–46. https://doi.org/10.4161/bioa.29069

23. N. C. Gauthier, O. M. Rossier, A. Mathur, J. C. Hone, M. P. Sheetz, Plasma membrane area increases with spread area by exocytosis of a gpi-anchored protein compartment, *Mol. Biol. Cell*, **20** (2009), 3261–3272. https://doi.org/10.1091/mbc.e09-01-0071

24. N. C. Gauthier, T. A. Masters, M. P. Sheetz, Mechanical feedback between membrane tension and dynamics, *Trends in Cell Biology*, **22** (2012), 527–535. https://doi.org/10.1016/j.tcb.2012.07.005

25. M. Goudarzi, K. Tarbashevich, K. Mildner, I. Begemann, J. Garcia, A. Paksa, et al., Bleb expansion in migrating cells depends on supply of membrane from cell surface invaginations, *Dev. Cell*, **43** (2017), 577–587. https://doi.org/10.1016/j.devcel.2017.10.030

26. N. C. Gauthier, M. A. Fardin, P. Roca-Cusachs, M. P. Sheetz, Temporary increase in plasma membrane tension coordinates the activation of exocytosis and contraction during cell spreading, *Proc. Natl. Acad. Sci. U.S.A.*, **108** (2011), 14467–14472. https://doi.org/10.1073/pnas.1105845108

27. B. Pontes, P. Monzo, L. Gole, A. L. Le Roux, A. J. Kosmalska, Z. Y. Tam, et al., Membrane tension controls adhesion positioning at the leading edge of cells, *J. Cell Biol.*, **216** (2017), 2959–2977. https://doi.org/10.1083/jcb.201611117

28. N. Nisenholz, K. Rajendran, Q. Dang, H. Chen, R. Kemkemer, R. Krishnan, et al., Active mechanics and dynamics of cell spreading on elastic substrates, *Soft Matter*, **10** (2014), 7234–7246. https://doi.org/10.1039/C4SM00780H

29. Z. Gong, S. E. Szczesny, S. R. Caliari, E. E. Charrier, O. Chaudhuri, X. Cao, et al., Matching material and cellular timescales maximizes cell spreading on viscoelastic substrates, *Proc. Natl. Acad. Sci. U.S.A.*, **115** (2018), E2686–E2695. https://doi.org/10.1073/pnas.1716620115

30. F. J. Vernerey, M. Farsad, A mathematical model of the coupled mechanisms of cell adhesion, contraction and spreading, *J. Math. Biol.*, **68** (2014), 989–1022. https://doi.org/10.1007/s00285-013-0656-8

31. E. G. Rens, R. M. Merks, Cell shape and durotaxis explained from cell-extracellular matrix forces and focal adhesion dynamics, *iScience*, **23** (2020), 101488. https://doi.org/10.1016/j.isci.2020.101488

32. E. McEvoy, S. S. Shishvan, V. S. Deshpande, J. P. McGarry, Thermodynamic modeling of the statistics of cell spreading on ligand-coated elastic substrates, *Biophys. J.*, **115** (2018), 2451–2460. https://doi.org/10.1016/j.bpj.2018.11.007

33. Y. Qin, Y. Li, L. Y. Zhang, G. K. Xu, Stochastic fluctuation-induced cell polarization on elastic substrates: A cytoskeleton-based mechanical model, *J. Mech. Phys. Solids*, **137** (2020), 103872. https://doi.org/10.1016/j.jmps.2020.103872

34. A. Zemel, F. Rehfeldt, A. Brown, D. Discher, S. Safran, Cell shape, spreading symmetry, and the polarization of stress-fibers in cells, *J. Phys.: Condens. Matter*, **22** (2010), 194110. https://doi.org/10.1088/0953-8984/22/19/194110

35. H. Fan, S. Li, Modeling universal dynamics of cell spreading on elastic substrates, *Biomech. Model. Mechanobiol.*, **14** (2015), 1265–1280. https://doi.org/10.1007/s10237-015-0673-1

36. M. Serpelloni, M. Arricca, C. Bonanno, A. Salvadori, Modeling cells spreading, motility, and receptors dynamics: a general framework, *Acta Mech. Sin.*, **37** (2021), 1013–1030. https://doi.org/10.1007/s10409-021-01088-w

37. M. Abu Hamed, A. A. Nepomnyashchy, Phase field model for cell spreading dynamics, *J. Math. Biol.*, **84** (2022), 1–15. https://doi.org/10.1007/s00285-022-01732-4

38. Y. Fang, K. W. Lai, Modeling the mechanics of cells in the cell-spreading process driven by traction forces, *Phys. Rev. E*, **93** (2016), 042404. https://doi.org/10.1103/PhysRevE.93.042404

39. Z. L. Zhao, Z. Y. Liu, J. Du, G. K. Xu, X. Q. Feng, A dynamic biochemomechanical model of geometry-confined cell spreading, *Biophys. J.*, **112** (2017), 2377–2386. https://doi.org/10.1016/j.bpj.2017.04.044

40. I. Lavi, M. Goudarzi, E. Raz, N. S. Gov, R. Voituriez, P. Sens, Cellular blebs and membrane invaginations are coupled through membrane tension buffering, *Biophys. J.*, **117** (2019), 1485–1495. https://doi.org/10.1016/j.bpj.2019.08.002

41. E. M. Craig, J. Stricker, M. Gardel, A. Mogilner, Model for adhesion clutch explains biphasic relationship between actin flow and traction at the cell leading edge, *Phys. Biol.*, **12** (2015), 1–15. https://doi.org/10.1088/1478-3975/12/3/035002

42. A. R. Bausch, F. Ziemann, A. A. Boulbitch, K. Jacobson, E. Sackmann, Local measurements of viscoelastic parameters of adherent cell surfaces by magnetic bead microrheometry, *Biophys. J.*, **75** (1998), 2038–2049. https://doi.org/10.1016/S0006-3495(98)77646-5

43. T. P. Stossel, Contribution of actin to the structure of the cytoplasmic matrix, *J. Cell Biol.*, **99** (1984), 15s–21s. https://doi.org/10.1083/jcb.99.1.15s

44. D. H. Wachsstock, W. Schwartz, T. D. Pollard, Affinity of alpha-actinin for actin determines the structure and mechanical properties of actin filament gels, *Biophys. J.*, **65** (1993), 205–214. https://doi.org/10.1016/S0006-3495(93)81059-2

45. B. J. Belin, L. M. Goins, R. D. Mullins, Comparative analysis of tools for live cell imaging of actin network architecture, *Bioarchitecture*, **4** (2014), 189–202. https://doi.org/10.1080/19490992.2014.1047714

46. P. Recho, L. Truskinovsky, Asymmetry between pushing and pulling for crawling cells, *Phys. Rev. E*, **87** (2013), 022720. https://doi.org/10.1103/PhysRevE.87.022720

47. M. E. Gracheva, H. G. Othmer, A continuum model of motility in ameboid cells, *Bull. Math. Biol.*, **66** (2004), 167–193. https://doi.org/10.1016/j.bulm.2003.08.007

48. R. I. Litvinov, A. Mekler, H. Shuman, J. S. Bennett, V. Barsegov, J. W. Weisel, Resolving two-dimensional kinetics of the integrin αiibβ3-fibrinogen interactions using binding-unbinding correlation spectroscopy, *J. Biol. Chem.*, **287** (2012), 35275–35285. https://doi.org/10.1074/jbc.M112.404848

49. L. Jiang, Z. Sun, X. Chen, J. Li, Y. Xu, Y. Zu, et al., Cells sensing mechanical cues: stiffness influences the lifetime of cell–extracellular matrix interactions by affecting the loading rate, *ACS Nano*, **10** (2016), 207–217. https://doi.org/10.1021/acsnano.5b03157

50. R. M. Hochmuth, N. Mohandas, P. Blackshear Jr, Measurement of the elastic modulus for red cell membrane using a fluid mechanical technique, *Biophys. J.*, **13** (1973), 747–762. https://doi.org/10.1016/S0006-3495(73)86021-7

51. E. Evans, R. Hochmuth, Membrane viscoelasticity, *Biophys. J.*, **16** (1976), 1–11. https://doi.org/10.1016/S0006-3495(76)85658-5

52. J. Barber, L. Zhu, Two-dimensional finite element model of breast cancer cell motion through a microfluidic channel, *Bull. Math. Biol.*, **81** (2019), 1238–1259. https://doi.org/10.1007/s11538-018-00557-x

53. E. A. Novikova, C. Storm, Contractile fibers and catch-bond clusters: a biological force sensor? *Biophys. J.*, **105** (2013), 1336–1345. https://doi.org/10.1016/j.bpj.2013.07.039

54. C. A. Copos, S. Walcott, J. C. Del Álamo, E. Bastounis, A. Mogilner, R. D. Guy. Mechanosensitive adhesion explains stepping motility in amoeboid cells, *Biophys. J.* **112** (2017), 2672–2682. https://doi.org/10.1016/j.bpj.2017.04.033

55. E. L. Barnhart, K. C. Lee, K. Keren, A. Mogilner, J. A. Theriot, An adhesion-dependent switch between mechanisms that determine motile cell shape, *PLoS Biol.*, **9** (2011), e1001059. https://doi.org/10.1371/journal.pbio.1001059

56. E. A. Cox, S. K. Sastry, A. Huttenlocher, Integrin-mediated adhesion regulates cell polarity and membrane protrusion through the rho family of gtpases, *Mol. Biol. Cell*, **12** (2001), 265–277. https://doi.org/10.1091/mbc.12.2.265

57. D. P. Choma, K. Pumiglia, C. M. DiPersio, Integrin $\alpha 3\beta 1$ directs the stabilization of a polarized lamellipodium in epithelial cells through activation of rac1, *J. Cell Sci.*, **117** (2004), 3947–3959. https://doi.org/10.1242/jcs.01251

58. E. S. Welf, H. E. Johnson, J. M. Haugh, Bidirectional coupling between integrin-mediated signaling and actomyosin mechanics explains matrix-dependent intermittency of leading-edge motility, *Mol. Biol. Cell*, **24** (2013), 3945–3955. https://doi.org/10.1091/mbc.E13-06-0311

59. A. Mehidi, O. Rossier, M. Schaks, A. Chazeau, F. Binamé, A. Remorino, et al., Transient activations of rac1 at the lamellipodium tip trigger membrane protrusion, *Curr. Biol.*, **29** (2019), 2852–2866. https://doi.org/10.1016/j.cub.2019.07.035

60. E. K. Rodriguez, A. Hoger, A. D. McCulloch, Stress-dependent finite growth in soft elastic tissues, *J. Biomech.*, **27** (1994), 455–467. https://doi.org/10.1016/0021-9290(94)90021-3

61. J. R. Rice, Continuum mechanics and thermodynamics of plasticity in relation to microscale deformation mechanisms, in *Constitutive Equations in Plasticity* (ed. A. S. Argon), MIT Press Cambridge, (1975), 23–79.

62. J. M. Kalappurakkal, A. A. Anilkumar, C. Patra, T. S. van Zanten, M. P. Sheetz, S. Mayor, Integrin mechano-chemical signaling generates plasma membrane nanodomains that promote cell spreading, *Cell*, **177** (2019), 1738–1756. https://doi.org/10.1016/j.cell.2019.04.037

63. C. K. Choi, M. Vicente-Manzanares, J. Zareno, L. A. Whitmore, A. Mogilner, A. R. Horwitz, Actin and α-actinin orchestrate the assembly and maturation of nascent adhesions in a myosin II motor-independent manner, *Nat. Cell Biol.*, **10** (2008), 1039–1050. https://doi.org/10.1038/ncb1763

64. P. Y. Jay, P. A. Pham, S. A. Wong, E. L. Elson, A mechanical function of myosin ii in cell motility, *J. Cell Sci.*, **108** (1995), 387–393. https://doi.org/10.1242/jcs.108.1.387

65. R. Meili, B. Alonso-Latorre, J. C. Del Alamo, R. A. Firtel, J. C. Lasheras, Myosin ii is essential for the spatiotemporal organization of traction forces during cell motility, *Mol. Biol. Cell*, **21** (2010), 405–417. https://doi.org/10.1091/mbc.e09-08-0703

66. B. Rubinstein, M. F. Fournier, K. Jacobson, A. B. Verkhovsky, A. Mogilner, Actin-myosin viscoelastic flow in the keratocyte lamellipod, *Biophys. J.*, **97** (2009), 1853–1863. https://doi.org/10.1016/j.bpj.2009.07.020

67. D. Shao, H. Levine, W. J. Rappel, Coupling actin flow, adhesion, and morphology in a computational cell motility model, *Proc. Natl. Acad. Sci. U.S.A.*, **109** (2012), 6851–6856. https://doi.org/10.1073/pnas.1203252109

68. A. Ponti, M. Machacek, S. L. Gupton, C. M. Waterman-Storer, G. Danuser, Two distinct actin networks drive the protrusion of migrating cells, *Science*, **305** (2004), 1782–1786. https://doi.org/10.1126/science.1100533

69. D. W. Dumbauld, H. Shin, N. D. Gallant, K. E. Michael, H. Radhakrishna, A. J. García, Contractility modulates cell adhesion strengthening through focal adhesion kinase and assembly of vinculin-containing focal adhesions, *J. Cell. Physiol.*, **223** (2010), 746–756. https://doi.org/10.1002/jcp.22084

70. S. Fusco, V. Panzetta, V. Embrione, P. A. Netti, Crosstalk between focal adhesions and material mechanical properties governs cell mechanics and functions, *Acta Biomater.*, **23** (2015), 63–71. https://doi.org/10.1016/j.actbio.2015.05.008

71. L. B. Case, C. M. Waterman, Integration of actin dynamics and cell adhesion by a three-dimensional, mechanosensitive molecular clutch, *Nat. Cell Biol.*, **17** (2015), 955–963. https://doi.org/10.1038/ncb3191

72. P. W. Oakes, S. Banerjee, M. C. Marchetti, M. L. Gardel, Geometry regulates traction stresses in adherent cells, *Biophys. J.*, **107** (2014), 825–833. https://doi.org/10.1016/j.bpj.2014.06.045

73. C. E. Chan, D. J. Odde, Traction dynamics of filopodia on compliant substrates, *Science*, **322** (2008), 1687–1691. https://doi.org/10.1126/science.1163595

74. Y. Cai, N. Biais, G. Giannone, M. Tanase, G. Jiang, J. M. Hofman, et al., Nonmuscle myosin iia-dependent force inhibits cell spreading and drives f-actin flow, *Biophys. J.*, **91** (2006), 3907–3920. https://doi.org/10.1529/biophysj.106.084806

75. W. S. Rasband, ImageJ, U. S. National Institutes of Health, Bethesda, Maryland, USA, (1997-2018). Available from: https://imagej.nih.gov/ij/.

76. E. Sitarska, A. Diz-Muñoz, Pay attention to membrane tension: mechanobiology of the cell surface, *Curr. Opin. Cell Biol.*, **66** (2020), 11–18. https://doi.org/10.1016/j.ceb.2020.04.001

77. J. Li, S. S. Wijeratne, T. E. Nelson, T. C. Lin, X. He, X. Feng, et al., Dependence of membrane tether strength on substrate rigidity probed by single-cell force spectroscopy, *J. Phys. Chem. Lett.*, **11** (2020), 4173–4178. https://doi.org/10.1021/acs.jpclett.0c00730

78. T. Wakatsuki, R. B. Wysolmerski, E. L. Elson, Mechanics of cell spreading: role of myosin ii, *J. Cell Sci.*, **116** (2003), 1617–1625. https://doi.org/10.1242/jcs.00340

79. D. E. Ingber, Tensegrity i. cell structure and hierarchical systems biology, *J. Cell Sci.*, **116** (2003), 1157–1173. https://doi.org/10.1242/jcs.00359

80. Y. Luo, X. Xu, T. Lele, S. Kumar, D. E. Ingber, A multi-modular tensegrity model of an actin stress fiber, *J. Biomech.*, **41** (2008), 2379–2387. https://doi.org/10.1016/j.jbiomech.2008.05.026

81. J. Kolega, Effects of mechanical tension on protrusive activity and microfilament and intermediate filament organization in an epidermal epithelium moving in culture, *J. Cell Biol.*, **102** (1986), 1400–1411. https://doi.org/10.1083/jcb.102.4.1400

82. D. E. Ingber, Tensegrity: the architectural basis of cellular mechanotransduction, *Annu. Rev. Physiol.*, **59** (1997), 575–599. https://doi.org/10.1146/annurev.physiol.59.1.575

83. J. M. Northcott, I. S. Dean, J. K. Mouw, V. M. Weaver, Feeling stress: the mechanics of cancer progression and aggression, *Front. Cell Dev. Biol.*, **6** (2018), 17. https://doi.org/10.3389/fcell.2018.00017

84. J. Stricker, Y. Beckham, M. W. Davidson, M. L. Gardel, Myosin II-mediated focal adhesion maturation is tension insensitive, *PLoS One*, **8** (2013), e70652. https://doi.org/10.1371/journal.pone.0070652

85. L. Trichet, J. Le Digabel, R. J. Hawkins, S. R. K. Vedula, M. Gupta, C. Ribrault, et al., Evidence of a large-scale mechanosensing mechanism for cellular adaptation to substrate stiffness, *Proc. Natl. Acad. Sci. U.S.A.*, **109** (2012), 6933–6938. https://doi.org/10.1073/pnas.1117810109

86. A. M. Greiner, H. Chen, J. P. Spatz, R. Kemkemer, Cyclic tensile strain controls cell shape and directs actin stress fiber formation and focal adhesion alignment in spreading cells, *PLoS One*, **8** (2013), e77328. https://doi.org/10.1371/journal.pone.0077328

87. G. A. Holzapfel, *Nonlinear Solid Mechanics: A Continuum Approach for Engineering*, Wiley and Sons, Chichester, 2000.

AIMS Press